Correcting for water vapor diffusion in air bag samples for isotope composition analysis: case study with drone-collected samples

Di Wang[1,2,3*], Camille Risi[2], Lide Tian[1], Di Yang[1], Gabriel J. Bowen[4], Siteng Fan[2,5],

Yang Su[6] , Hongxi Pang[7], Laurent Z.X Li[2]

[1] *Institute of International Rivers and Eco-security, Yunnan University, Yunnan Key Laboratory of International Rivers and Transboundary Eco–security, Kunming 650500, Yunnan, China*

[2] *Laboratoire de Météorologie Dynamique, IPSL, CNRS, Sorbonne Université, Campus Pierre et Marie Curie, Paris 75005, France*

[3] *Laboratoire Atmosphères, Observations Spatiales, IPSL, CNRS, UVSQ, Sorbonne Université, Guyancourt 78280, France*

[4] *Department of Geology and Geophysics, University of Utah, Salt Lake City, Utah 84108, USA*

[5] *Department of Earth and Space Sciences, Southern University of Science and Technology, Shenzhen 518055, China*

[6] *Département d'Informatique, École normale supérieure – PSL, 45 Rue d'Ulm, 75005 Paris, France*

[7] *Key Laboratory of Coast and Island Development of Ministry of Education, School of Geography and Ocean Science, Nanjing University, Nanjing 210023, China*

Corresponding author: di.wang@latmos.ipsl.fr; shidi.upmc@gmail.com

Abstract

Mass spectrometry and laser spectroscopy have been widely employed for precise water vapor isotope measurements. Nevertheless, these techniques are limited by logistical challenges in fieldwork, consequently constraining the temporal and spatial resolution of measurements. Specifically, water vapor isotope measurements are primarily limited to near-surface levels, while measurements in the free troposphere are notably scarce. Portable sampling devices, such as air bags and glass bottles, have therefore become necessary alternatives for collecting, storing, and transporting gaseous samples in diverse environments prior to analysis with less portable instruments. In drone-based high-altitude vapor sampling, air bags are preferred for their lighter weight and greater flexibility compared to glass bottles. Nevertheless, they present specific challenges, such as potential sample contamination and isotopic fractionation during storage, primarily due to the inherent permeability of air bags. Here, we developed a theoretical model for water vapor diffusion through the sampling bag surface, with parameters calibrated through laboratory experiments. This model enables the reconstruction of the initial isotopic composition of sampled vapor based on measurements obtained within the bag and from the surrounding environment. This diffusion model underwent rigorous validation through experiments conducted under varying humidity and isotopic composition differences between the inside and outside of the air bag, confirming its reliability. We applied this correction method to air samples collected at various pressures up to the upper troposphere using an air bag-mounted drone that we developed, thereby estimating the initial isotopic composition and uncertainty based on our observations. ~~The corrected observations match the Picarro in situ observations and IASI satellite retrievals.~~ Our correction method enhances the reliability and applicability of water vapor isotope observations conducted using drones equipped with air bags, and provides a detailed assessment of all potential sources of error and quantifies the uncertainty range of the observations. This approach leverages the strengths of drone-based air bag sampling while mitigating its limitations, thus facilitating the convenient collection of isotopic data throughout the troposphere.

1 Introduction

Water vapor isotopes provide unique insights into the transport, mixing, and phase changes of water in the environment, which are crucial for improving understanding of the climate system, hydrological cycle, atmospheric dynamics, and paleoclimate proxies. Water isotopes have also been applied in climate modeling, weather prediction, and water resource management (Bowen et al., 2019; Galewsky et al., 2016; Gat, 1996; West et al., 2009).

Water isotope analysis has traditionally relied on mass spectrometry, which, while accurate (Ghosh and Brand, 2003; Muccio and Jackson, 2009), demands labor-intensive preparation and lacks portability (West et al., 2010). Methods like cryogenic trapping effectively collect water vapor (Grootes and Stuiver, 1997; Michener and Lajtha, 2008; Steen-Larsen et al., 2011; Yu et al., 2015), but they require long sampling periods, limiting observation scope and timing. Over the past three decades, laser spectroscopy methods such as Cavity Ring-Down Spectroscopy (CRDS)(Hodges and Lisak, 2006) and Off-Axis Integrated Cavity Output Spectroscopy (OA-ICOS) (Johnson et al., 2011) have emerged, delivering a best-in-class combination of speed, high precision, and continuous measurements even in challenging environments such as high altitudes or arid regions with low water vapor content. Advances in these instruments have significantly expanded the field of water isotope research. However, their heavy instrumentation, substantial power requirements, and limited mobility restrict their usability in certain situations, particularly for aerial water vapor isotope measurements, which require lightweight and flexible sampling approaches. As a result, the collection and storage of physical samples are still necessary, increasing the demand for more convenient and efficient sample acquisition methods. Air bags and glass bottles have been practical solutions for collecting, storing, and transporting gaseous samples from various settings (Rozmiarek et al., 2021).

Given that air bags can reduce the weight of sampling equipment and increase sampling flexibility, there is considerable interest in using them for vapor sample collection. This is particularly advantageous for small equipment like drones, where minimizing payload weight is essential for sampling at high altitudes or over long distances. This selection also makes it easier to transport samples and reduces the risk of breakage. However, concerns have arisen regarding the suitability of various sampling materials for storing these samples, primarily due to potential water diffusion through container walls. Diffusion issues are commonly observed in sampling bags during water vapor isotope analysis and have persisted as a longstanding challenge in the field (Gralher et al., 2021; Havranek et al., 2020; Herbstritt et al., 2023; Magh et al., 2022). In previous studies, this issue is particularly concerning in the Direct Vapor Equilibrium Laser Spectroscopy (DVE-LS) method, which has been widely used to rapidly collect and measure water isotopes in evaporation-prone soil, rock, or plant samples. The DVE-LS method simplifies preparation and increases sample throughput by directly analyzing the vapor phase, thus eliminating the need for extensive physical extractions (Gralher et al., 2021; Hendry et al., 2015; Millar et al., 2018; Sprenger et al., 2015; Wassenaar et al., 2008). However, water vapor molecules may exchange between the air inside the bag and the external ambient air during sample storage. Water vapor molecules typically diffuse from areas of high humidity to drier areas. In this process, heavier isotopologues (e.g., $H_2^{18}O$ and HDO) move more slowly than lighter isotopologues (e.g., $H_2^{16}O$) due to their greater mass, resulting in preferential

92 diffusion of lighter isotopes. This differential diffusion, can alter the original isotopic
93 composition of the collected air samples. Moreover, differential diffusion can also occur due to
94 gradients in isotopic composition.

95 To mitigate these issues, specific diffusion-tight materials are highly recommended for
96 water vapor isotope measurements, although adsorption effects may still occur with such
97 materials(Herbstritt et al., 2023). Further research and development are still necessary. This
98 may involve exploring alternative materials for more impermeable sampling bags, improving
99 sealing methods to better isolate sampled air, and developing sampling techniques less
100 susceptible to diffusion. Resolving these issues is essential for ensuring the reliability of water
101 vapor isotope measurements using air bags and for accurately understanding atmospheric and
102 hydrological processes.

103 In light of the ongoing development and further refinement of these techniques and the
104 associated cost constraints, we developed a diffusion model with parameters calibrated through
105 laboratory experiments. This model is capable of assessing the permeability of the air bags and
106 correcting the obtained isotope measurements to the initial pre-diffusion values based on the
107 humidity, isotope values inside and outside the bag, and the sample storage time. This diffusion
108 model was validated through experiments under varying humidity and isotopic composition
109 differences between the inside and outside of the air bag, confirming its reliability. Furthermore,
110 we also applied this diffusion method to air samples collected at different altitudes using a
111 drone-based atmospheric vapor sampling device we developed, to estimate the initial isotope
112 composition and uncertainty. The primary objective of this drone-based field campaign is to
113 obtain atmospheric water vapor isotope data along vertical profiles in the troposphere,
114 providing higher temporal and spatial resolution than satellite observations. The corrected near-
115 surface drone-based measurements using our diffusion model show improved consistency with
116 direct, in-situ surface-level measurements using the Picarro analyzer. ~~Similarly, at two mid-~~
117 ~~tropospheric levels, the corrected drone measurements align with IASI satellite observations of~~
118 ~~water vapor isotopic composition, further confirming the model's theoretical and reliability in~~
119 ~~applications.~~ Our model, validated by laboratory experiments under a wide range of
120 environmental conditions, was used to assess all potential error sources and to quantify a
121 conservative, comprehensive uncertainty range for the corrected vertical profiles. Although we
122 minimized certain diffusion-related biases, such as pressure in different altitudes and long
123 storage times, temperature and the pressure difference between the inside and outside of the
124 bags on bag permeability were only addressed indirectly via conservative uncertainty estimates.
125 This treatment is justified under our experimental conditions, which are characterized
126 by~~However, because of~~ the short residence time at high altitudes, the reduced diffusivity at low
127 temperatures, and the flexibility of the bags maintaining equal internal and external pressure~~,~~
128 ~~our current approach does not explicitly resolve potential temperature- or pressure-dependent~~
129 ~~changes in bag permeability. Under our experimental conditions, these effects were instead~~
130 ~~addressed indirectly through conservative uncertainty estimates.~~ Future applications should
131 ~~take into account~~consider the specific experimental conditions, and future developments may
132 extend the model to explicitly incorporate the dependence of bag permeability on partial
133 pressure and temperature, thereby improving its applicability under a wider range of
134 atmospheric conditions.

2 Theoretical basis of diffusion model

2.1 Diffusion model description

Storing vapor samples in air bags prior to isotope measurement may alter the isotopic composition of the water vapor. The main reason is the diffusion of water molecules between the interior and exterior of the air bags, primarily due to the permeability of the bag materials. We present a mathematical model for the diffusion and fractionation of isotopes across the surface of the sampling bag. In this model, we assume the ambient vapor flux entering the air bag changes the internal humidity and vapor isotopic composition, influenced by the different humidity and water isotopic composition inside and outside the bag (Fig.1).

The flux of water into the bag, F (in kg/m^2/s), is expressed as:

$$F = k * (q_e - q(t)) \tag{1}$$

where $q(t)$ represents the variation of humidity inside the air bag over time (in kg/kg), q_e denotes the environmental humidity (in kg/kg), k is water vapor conductance. This first-order formulation is derived from Fick's diffusion law(Fick, 1855).

Similarly, the flux of isotopologue, F_i, either $H_2^{18}O$ or HDO, moving into the bag can be described as:

$$F_i = k_i * (R_e * q_e - R(t) * q(t)) \tag{2}$$

In this equation, k_i represents the conductance specific to each isotopologue (in kg/m^2/s), R_e denotes the isotopic ratio in the environment, and $R(t)$ is the variation of isotopic ratio within the air bag with time. Notably, the fractionation coefficient here can be denoted as:

$$\alpha = \frac{k}{k_i} \tag{3}$$

Since k represents the total ~~conductance~~ ~~flux~~ dominated by the lighter molecules ($H_2^{16}O$)~~including both light and heavy molecules~~, and k_i is defined as the conductance of the heavier isotopologues (either $H_2^{18}O$ or HDO)~~it is approximated as the conductance of the heavy molecules (k_{heavy})~~, ~~so that~~ Eq. (3) is therefore consistent with the conventional definition of fractionation factors ($\alpha = \frac{k_{heavy}{\scriptstyle light}}{k_{light}{\scriptstyle heavy}}$).

The validity of Eqs.1 and 2 relies on the assumptions that internal and external pressures remain equal to atmospheric pressure, ensuring no pressure gradient across the bag membrane, that the internal vapor is well-mixed, and that the exchange rate follows a first-order process. Additionally, if the temperature remains constant, k and k_i are assumed to be constant.

Assuming that diffusion through the bag is the primary transport mechanism, and neglecting adsorption, the temporal change in humidity can be modeled by the following differential equation:

$$\frac{d(q(t) * M)}{dt} = F * A \tag{4}$$

where A represents the exchange area (surface area of the air bag), and M is the air mass inside the bag.

Assuming that M is constant, which is reasonable given that the total mass variation due

173 to water vapor flux is at most 1%, this equation simplifies to:

174
$$\frac{dq(t)}{dt} = \frac{F*A}{M} = \frac{k*A}{M} * (q_e - q(t)) \tag{5}$$

175 Here, we define the water vapor exchange coefficient as follows, it describes the rate at
176 which water vapor exchanges across the bag membrane:

177
$$\lambda = \frac{k*A}{M} \tag{6}$$

178 Similarly, the temporal change in isotopic ratio can be modeled by the following
179 differential equation:

180
$$\frac{d(R(t)*q(t)*M)}{dt} = M * (q(t) * \frac{dR(t)}{dt} + R(t) * \frac{dq(t)}{dt})$$

181
$$= F_i * A = k_i * (R_e * q_e - R(t) * q(t)) * A \tag{7}$$

182 This equation can be simplified as:

183
$$\frac{dR(t)}{dt} = \frac{k_i*(R_e*q_e-R(t)*q(t))*A/M - R(t)*\frac{dq(t)}{dt}}{q(t)}$$

184
$$= \frac{\frac{k*A}{M*\alpha}*(R_e*q_e-R(t)*q(t)) - R(t)*\frac{k*A}{M}*(q_e-q(t))}{q(t)}$$

185
$$= \frac{\frac{\lambda}{\alpha}*(R_e*q_e-R(t)*q(t)) - R(t)*\lambda*(q_e-q(t))}{q(t)}$$

186
$$= \frac{\lambda}{\alpha} * (R_e - R(t)) + \frac{\lambda}{q(t)} * (q_e - q(t)) * (\frac{R_e}{\alpha} - R(t)) \tag{8}$$

187

188 If q_e is stable (the environment is treated as an infinite reservoir), and that k and A are
189 constant, the differential equation for humidity (Eq. 5) can be analytically solved:

190
$$q_e - q(t) = (q_e - q_0) * e^{(-\frac{k*A}{M}*t)} = (q_e - q_0) * e^{(-\lambda*t)} \tag{9}$$

191 where q_0 is the initial humidity at t = 0. This equation can also be expressed in terms of
192 natural logarithms as:

193
$$\ln(q_e - q(t)) = \ln(q_e - q_0) - \lambda * t \tag{10}$$

194 Consequently, the slope of $\ln(q_e - q(t))$ against time is λ.

195

196 For the isotopic ratio, the analytical solution is only feasible when the initial humidity
197 equals the environmental humidity ($q_0 = q_e$):

198
$$\frac{dR(t)}{dt} = \frac{k*A}{M*\alpha} * (R_e - R(t)) \tag{11}$$

199 Assuming that R_e, q_e, k, α and A are constant:

200
$$\text{Thus, } R_e - R(t) = (R_e - R_0) * e^{(-\frac{k*A}{M*\alpha}*t)} \tag{12}$$

201 where R_0 denotes the initial isotopic ratio at t = 0. Again, taking the natural logarithm, we
202 obtain:

203
$$\ln(R_e - R(t)) = \ln(R_e - R_0) - \frac{\lambda}{\alpha} * t \tag{13}$$

204 This equation demonstrates that the slope of $\ln(R_e - R(t))$ against time is the water vapor

205 isotopic exchange coefficient $\frac{\lambda}{\alpha}$. Knowing λ, we can deduce the isotopic fractionation

206 coefficient α for each isotope.

207 However, when the environmental humidity differs from the initial humidity inside the air
208 bag, a numerical solution is required to solve the differential equation for R (Eq. 8).

209
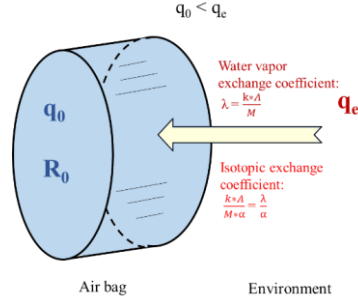
Figure 1 Schematic illustrating the diffusion model. q_0 *represents the initial humidity in the air bag at t = 0,* q_e *denotes the environmental humidity,* R_0 *indicates the initial isotopic ratio in the air bag at t = 0,* R_e *represents the isotopic ratio in the environment, k is water vapor conductance, A denotes the exchange area (surface area of the bag), and M is the mass of air within the bag, and* α *denotes the isotopic fractionation coefficient.*

210 ### 2.2 Reconstructing initial water vapor isotopic compositions

211 The isotopic composition of the air bag water vapor undergoes an exponential evolution
212 over time (Eq. 12). This method of applying exponential evolution equations to reconstruct
213 isotopic compositions has been used in environmental forensics to investigate shifts in water
214 isotopes due to metabolic changes, environmental conditions, or diet (Ayliffe et al., 2004;
215 Cerling et al., 2006). Similarly, in climatology, this method helps retrieving initial isotopic
216 composition from samples such as ice cores or tree rings, affected by evaporation, precipitation,
217 and temperature fluctuations, facilitating historical climate reconstruction (Brienen et al., 2016).
218 Here we apply a similar method, and apply the analytical solution of Eq.8 using data from
219 experiments in which the condition that q_0 equals q_e is met to determine the equation parameters.
220 The constants (λ, α$-^{18}$O, α$-^2$H) can be determined through laboratory experiments and Eqs.
221 10 and 13 (see Subsection 3.2 and 4.1). If we know the initial values within the air bag (q_0,
222 R$-^{18}$O$_0$, R$-^2$H$_0$), the ambient values (q_e, R$-^{18}$O$_e$, R$-^2$H$_e$) during storage (approximated using
223 ground-level conditions), and the storage time after sampling (T$-_{storage}$), we are able to simulate
224 the variations in humidity and isotopic ratios inside the air bag according to Eqs. 5 and 8.
225 Similarly, if we know T$-_{storage}$, the humidity and isotopic composition at time t = T$-_{storage}$
226 ($q_{(T-storage)}$, R$-^{18}$O$_{(T-storage)}$, R$\_^2$H$_{(T-storage)}$) in the air bag, and the ambient values, we can deduce
227 the initial values in the air bag at t = 0 by back-calculating. The equation used for reconstructing
228 the initial isotope ratio (R_0) is:

229
$$R_0 = R_{measured} - \int_0^{T_{storage}} \frac{dR(t)}{dt} dt$$

230
$$= R_{measured} - \int_0^{T_{storage}} \left(\frac{\lambda}{\alpha} * \left(R_e - R(t) \right) + \frac{\lambda}{q(t)} * \left(q_e - q(t) \right) * \left(\frac{R_e}{\alpha} - R(t) \right) \right) dt \quad (14)$$

231 where R_0 represents the initial isotopic ratio to be reconstructed, R$-_{measured}$ is the observed

232   isotopic ratio after $T_{storage}$, and $\frac{dR(t)}{dt}$ is defined in Eq. 8.

233   This approach allows us to correct for diffusion-induced isotopic shifts and reconstruct the
234 original vapor composition.

235   For mathematical clarity and consistency, isotopic ratios (R) are used in the equations
236 presented in previous sections. Replacing R with δ-values would only shift the physical basis
237 without affecting the mathematical validity of the equations or the estimation of α, as the
238 standard ratio cancels out. For clearer visualization, δ-values are used for numerical
239 applications and in the subsequent figures and tables.

240   The δ and d-excess values used in this study follow standard definitions:

$$\delta^{18}O \ = \left(\frac{R^{18}O_{sample}}{R^{18}O_{standard}} - 1\right) * 1000 \tag{15}$$

$$\delta^{2}H \ = \left(\frac{R^{2}H_{sample}}{R^{2}H_{standard}} - 1\right) * 1000 \tag{16}$$

$$d - excess = \ \delta^{2}H - 8 * \delta^{18}O \tag{17}$$

244   Here, $R^{18}O_{standard} = 2.0052*10^{-3}$ and $R^{2}H_{standard} = 1.5576 * 10^{-4}$, corresponding to
245 the VSMOW international reference values.

3   Methods and data

3.1   Air bag isotope measurements
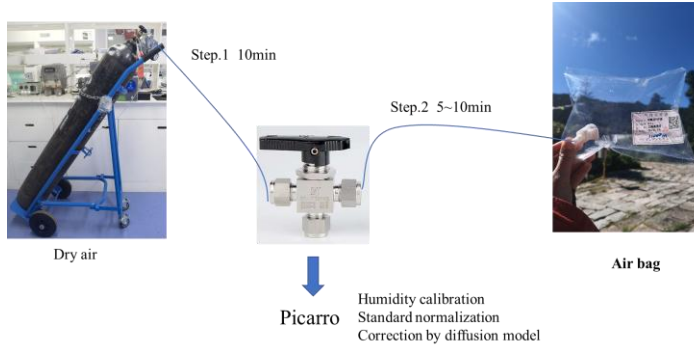
Figure 2 Setup for isotope measurements using air bags with a Picarro atmospheric water vapor isotope analyzer.

248   In this study, we used 0.5 L and 4 L Teflon air bags produced by Dalian Hede Technologies
249 Co., Ltd to collect and store vapor, and measured the vapor isotopes using a Picarro 2130i water
250 isotope analyzer. Based on our testing and the airflow rate set for the Picarro analyzer, the 0.5
251 L and 4 L bags provided sufficient sample volume for approximately 17 minutes and 130
252 minutes of analysis, respectively.

253   Figure 2 illustrates the setup for measuring vapor isotopes in air bags. In this system, the
254 air inlet of the Picarro isotope analyzer was connected to a three-way valve through Teflon or
255 stainless-steel tubing. The other two ports of the three-way valve were attached to the outlet
256 valve of the air bag and a dry air cylinder, respectively. Sample storage and measurement were
257 conducted in a temperature-regulated room to maintain constant temperature conditions for the
258 air bags and tubing.
259   In the measurement procedure, we first activated the dry air cylinder and adjusted the
260 pressure reducing valve to 13.8 kPa (2 psi,pounds of force per square inch), within the Picarro
261 water isotope analyzer's recommended range of 13.8–27.6 kPa (2–4 psi) for carrier gas. The
262 instrument's built-in flow regulation maintains a gas flow rate of 40 sccm at 760 Torr,
263 corresponding to ~ 30–50 mL/min in our measurement conditions, ensuring stable sample
264 delivery. We then opened the valve channel connecting the dry air cylinder to the three-way
265 valve, allowing dry air to flow into the isotope analyzer and flush all air pathways for 10
266 minutes. Subsequently, we closed the dry air channel, opened the air bag outlet valve, and the
267 corresponding valve channel on the three-way valve. This allowed water vapor in the air bags
268 to be analyzed at a constant temperature in the Picarro analyzer, a process lasting between 5
269 and 10 minutes. Upon completion, we switched the valve to measure dry air. By repeatedly
270 measuring isotopic composition for replicate samples—air samples collected simultaneously
271 under the same conditions—we ensured the consistency of the water vapor measurements.
272   To correct isotope measurement bias caused by the instrument's sensitivity to different
273 water vapor concentrations (Schmidt et al., 2010), we used the built-in Standard Delivery
274 Module (SDM) of the Picarro L2130-i water vapor isotope analyzer to generate a 500–25,000
275 ppm water vapor gradient for isotope measurements. We selected 20,000 ppm as a reference
276 humidity level, as this corresponds to the optimal accuracy range of the Picarro analyzer
277 (JingfengLiu et al., 2014; Schmidt et al., 2010). All the measured vapor isotope data were
278 normalized to the VSMOW-SLAP scale using two distinct laboratory reference waters with
279 known isotopic composition. Before conducting daily measurements, we adjusted the quantity
280 of the injected liquid standard to align with the humidity of the external vapor measurements.

3.2 Laboratory permeability experiments

282   To evaluate the variations of the diffusion of water molecules between the interior and
283 exterior of the air bags, we conducted the following experiments (Table A1), as detailed below:

3.2.1   Experiment No. 1: Quantification of $\lambda_{surface}$

285   To quantify the water vapor exchange coefficient at the surface, $\lambda_{surface}$, using Eq.10, we
286 filled the empty and clean air bags with dry air and measured humidity variations using a
287 Picarro analyzer at intervals of 1 minute, 2, 4, 6, 8, and 10 hours following the measurement
288 method described in Subsection 3.1. As λ is related to the ~~exchange area (~~surface area of the
289 ~~air~~sampling bag~~)~~, measurements were conducted using 0.5L and 4L air bags, with repetitions
290 on both identical and different air bags of the same dimensions (refer to the experiment times
291 in Table 1 and results in Fig.3a). We measured $\lambda_{surface}$ (=k*A/M) under near-surface pressure
292 and temperature we set in a controlled chamber. While k may vary with temperature and

293 pressure, these effects were assumed negligible within the condition of our study. Results will
294 be shown in Subsection 4.1.

3.2.2 Experiment No. 2: Quantification of α

296   To investigate isotope variation patterns and improve measurement accuracy during
297 storage in the air bag to quantify the isotopic fractionation coefficient α, using Eq.13, initial
298 values significantly different from ambient conditions were selected. Empty, clean air bags
299 were first filled with dry air, then sealed by closing the bag valve. To maintain a closed system
300 while injecting reference water, a dedicated injection septum was installed on the valve. After
301 reopening the valve, a fixed amount of laboratory reference liquid water with known isotopic
302 composition was injected into the dry air-filled bag using a 10 μL injection needle. In
303 Experiment No. 2, we ensured that the initial humidity (q_0) was approximately equal to the
304 environmental humidity (q_e). To ensure $q_0 = q_e$, the environmental vapor concentration was first
305 measured, followed by the calculation and experimental determination of the water volume to
306 be injected into the air bag. Water vapor concentration and isotope variations within the air bags
307 were then measured using a Picarro analyzer at intervals of 5 minutes, 2, 4, 6, 8, and 10 hours.
308 Results will be shown in Subsection 4.1. To ensure data consistency and reliability, we repeated
309 these measurements multiple times using air bags of both the same and different sizes, including
310 0.5L and 4L bags. For the 0.5L air bags, a separate bag was prepared for each time interval, and
311 water vapor concentration and isotopic compositions were measured once to ensure that the
312 parameter M remained stable without being affected by repeated measurements. However,
313 manual injection of reference water with known isotopic composition introduced some
314 variability, causing minor variations in initial values across all bags. This is evident in Figs 5,
315 6, and A2, where $q_0 = 1/2\, q_e$ data exhibit slight fluctuations due to the use of separate bags for
316 each time interval. To address this, we repeated the experiment with 4L air bags, measuring the
317 same air bag at different time intervals, which ensured consistent initial conditions at t=0 but
318 allowed M to change over time. When air bags differ only in size, the parameter λ associated
319 with A and M varies, while the isotopic fractionation coefficient α is theoretically constant.
320 Both approaches could contribute to uncertainties in the mismatches between the model and
321 experimental results. Therefore, we incorporated the results from both the 0.5 L and 4 L
322 experiments into our uncertainty estimation of these mismatches, as detailed in Subsections
323 3.2.3 and 3.4.2.

3.2.3 Experiment No. 3: Diffusion model validation

325   To validate the diffusion model under diverse conditions and evaluate its uncertainties, we
326 repeated Experiment No. 2, but injected different amounts of water with known isotopic
327 composition to achieve a range of humidities from approximately $1/8 * q_e$ to q_e. Using the
328 method described in Experiment No. 2, we injected 6 to 50 μL of reference water into a 4L air
329 bag filled with dry air to achieve the desired humidity range. Additionally, we repeated the
330 experiment using two reference waters with distinct isotopic compositions, specifically $\delta^{18}O =$
331 -58.07‰, $\delta^2H = -447.41$‰ and $\delta^{18}O = -29.84$‰, $\delta^2H = -222.84$‰. To assess extended-duration
332 variations, we also lengthened the time interval to 24 hours.

333   Once the parameters of the diffusion model have been obtained through Experiments No.
334   1 and 2, we used this model to simulate the variations in water vapor humidity and isotopic
335   composition inside the air bag over time for Experiments No. 2 and 3 (refer to Section 2). When
336   simulating these experiments using the diffusion model, we used measurements taken after a
337   5-minute delay as the initial condition to ensure that it represented complete evaporation of the
338   injected water. We then simulated the temporal variations in humidity and vapor isotopes within
339   the air bag using a 5-minute time step using Eqs. 5 and 8, separately. The resulting outputs
340   (hereafter referred to as 'the diffusion model simulations') will be shown in Subsection 4.2 and
341   code are available as supplementary material.

342   3.3 **Drone-mounted systems and field campaign**

343   We designed and built a collection module for fixed-height sampling, incorporating
344   diaphragm vacuum pumps, a rudder mounted on the drone, and a control module linked to a
345   remote operating system. Before flight, each air bag was evacuated on the ground using the
346   diaphragm pumps. When inactive, these self-sealing pumps effectively isolated the interior of
347   the air bags from the external environment, minimizing diffusion prior to sampling. When the
348   drone reaches a specified altitude, we remotely activate the designated air pump to inflate a
349   specific air bag. Once sampling is complete, the pump is deactivated, and the drone ascends to
350   the next target altitude, where the corresponding air pump inflates another air bag. This process
351   was repeated until all predetermined samples were collected. After each sampling, the pump
352   remained sealed, ensuring no unintended air ingress during descent~~, preventing unintended air~~
353   ~~ingress~~. Additionally, due to the flexible nature of the air bags, internal and external pressures
354   remained balanced. As air pressure increases during the drone's descent after collection. To
355   further prevent the loss of collected air samples, a one-way valve was installed to block
356   backflow. Additionally, the one-way valve helps prevent large droplets from entering the air
357   bag during the collection process.
358   The sampling module was mounted on our specially designed high-altitude drones and
359   deployed during a field campaign conducted from June 25, 2020, to October 17, 2020, in the
360   pristine forests of Mountain Laojun, Lijiang, on the southeastern edge of the Tibetan Plateau
361   and the northwestern of the Yunnan-Guizhou Plateau, China. We collected water vapor samples
362   every 500 meters, starting from near the surface along the vertical profile. To optimize sampling
363   across different altitude ranges, we deployed UAVs designed for varying flight altitudes.
364   Generally, the UAV operating at lower altitudes collected samples at seven heights from 4,000
365   to 7,000 meters in a single flight. The mid-altitude UAV collected samples at four heights from
366   7,500 to 9,000 meters in one flight, while the high-altitude UAV collected samples at four
367   heights from 9,500 to 11,000 meters in two flights. Each flight took approximately 20~30
368   minutes. In case of any disruptions during sampling, we repeated the process until a complete
369   vertical profile was obtained. At the beginning of the experiment, we also collected replicate
370   samples at each height to ensure data consistency.
371   By integrating high-altitude drone sampling with subsequent water vapor isotope analysis
372   using the Picarro analyzer at the surface, we obtained vapor isotopic profiles up to an altitude
373   of 11 km. Unlike conventional methods, such as cryogenic vapor sampling, this approach
374   requires much less sample volume and allows for timely measurements. Additionally, compared

375 to large aircraft, airships, and balloon-based observations, this method is relatively low-cost
376 and supports more flexible and long-term observations.

3.4 Application of diffusion model to vertical profiles

3.4.1 Estimating the air mass in the bag

379 λ is defined as k*A/M and depends on the air mass M in the bag. In drone-based vertical
380 sampling, M varies with altitude due to pressure changes, requiring an estimate of λ for different
381 altitudes (λ_{alt}). However, since λ is an intrinsic property of the bag material, its apparent
382 variation reflects uncertainties in estimating collected M, which depend on atmospheric
383 pressure (P), sampling time, and pump efficiency (ε):

384 $$M_{alt} = M_{surface} * \frac{P_{surface}}{P_{alt}} * \frac{Sampling\ time_{alt}}{Sampling\ time_{surface}} * \varepsilon \qquad (15)$$

385 where M_{alt} is the air mass collected at a different altitude and $M_{surface}$ represents the air
386 mass collected at the surface. At higher altitudes, where the air pressure (P_{alt}) is lower than at
387 the surface ($P_{surface}$), less air will be pumped into the air bag. To compensate for this effect, a
388 longer sampling time was used to collect air at higher altitudes (Sampling time$_{alt}$) than at the
389 surface (Sampling time$_{surface}$) (Fig.A1).

390 Given that λ_{alt} is proportional to M_{alt}, we calculated it as:

391 $$\lambda_{alt} = \lambda_{surface} * \frac{P_{surface}}{P_{alt}} * \frac{Sampling\ time_{alt}}{Sampling\ time_{surface}} * \varepsilon \qquad (16)$$

392 where $\lambda_{surface}$ is the λ quantified experimentally at the surface.

393 Since air pressure and sampling times were directly measured, the primary source of error
394 for M_{alt}, and consequently λ_{alt}, arises from pump efficiency (ε), which may decrease over time
395 and at lower pressures. Using the estimated λ_{alt}, the observed vertical isotope profiles were
396 corrected based on Eq.14 from Section 2.2. The uncertainty estimation is discussed in Section
397 3.4.2.

3.4.2 ~~The m~~Method of uncertainty estimation

399 Potential errors in correcting vertical profiles using the diffusion model include estimates
400 of $\lambda_{surface}$, α, pump efficiency (ε), and mismatches between model and experiments (Table 1).
401 We detail each below:
402 1) $\lambda_{surface}$ uncertainty: laboratory experiments provided upper and lower bounds on $\lambda_{surface}$
403 (Subsection 4.1). These were used for error estimation.
404 2) α uncertainty: the λ and λ/α were first estimated from several experiments, from which
405 α was calculated. Their averaged values were used separately to parameterize the model. As
406 highlighted in Subsection 3.2.2, estimating λ/α (and subsequently calculating α) requires results
407 from cases where q_0 equals q_e, minor variations in q_0 and fluctuations in q_e could introduce non-
408 systematic discrepancies between the model and experimental results. Consequently, for
409 analyzing the contribution of α to uncertainties, only α derived from experiments where the
410 model closely matched the majority of experimental results were considered. Selection criteria

411   for these experiments included minimal deviation between q_0 and q_e, minimal deviation
412   between experimental data and simulations, and stable q_e, ensuring the reliability of the chosen
413   α.
414   3) Pump efficiency (ε) uncertainty: The efficiency of the pump may decline over time or
415   vary with atmospheric pressure, affecting the collected air mass M. To account for this, we
416   applied a conservative uncertainty range of 0.75 to 1.25 relative to surface conditions, ensuring
417   the full range of possible variations in M_{alt} was considered.
418   4) Model-experiment mismatches: We compared model simulations with experimental data
419   across 87 cases, calculating the average absolute discrepancy. These mismatches were included
420   as an additional uncertainty component.
421   Total Uncertainty Calculation: The maximum discrepancy across all calibration results—
422   using the full uncertainty range for $\lambda_{surface}$, α, and pump efficiency (ε)—was determined. The
423   model-experiment mismatch was then added as an independent error component. The final
424   uncertainty estimates, reported in Subsections 4.3 to 4.5, account for all potential error.

Table 1 Uncertainties and estimation methods

Uncertainties	Number of experiments	Estimation method	Used value (min~max for error estimation)
$\lambda_{surface}$	7 (0.5L bags); 6 (4L bags)	Obtained from lab experiments (max & min)	For 0.5L air bags: 0.031(0.0291~0.0317); For 4L air bags: 0.0255(0.0250~0.0259)
α	4	Obtained from lab experiments	α–^{18}O is 1.0241, α–^{2}H is 1.0451 (α–^{18}O is 1.0254, α–^{2}H is 1.0506 and α–^{18}O is 1.0264, α–δ^{2}H is 1.0380)
Pump efficiency (ϵ)	-	0.75~1.25 relative to surface conditions	0.75~1.25
Mismatches between model and experiments	87	Average of all differences between experimental data and simulations	0.5 ‰ for δ^{18}O, 4.1 ‰ for δ^{2}H, 2.9 ‰ for d-excess

425   ### 3.5 Satellite isotope data from IASI

426   Several satellite missions have contributed to water vapor isotope observations, including
427   the Tropospheric Emission Spectrometer (TES) onboard Aura (2004–2018) (Worden et al.,
428   2006), the Scanning Imaging Absorption Spectrometer for Atmospheric Cartography
429   (SCIAMACHY) onboard Envisat (2002–2012), the Atmospheric Infrared Sounder (AIRS)
430   onboard Aqua (since 2002) (Worden et al., 2019), and the Tropospheric Monitoring Instrument
431   (TROPOMI) onboard Sentinel 5 Precursor (since 2017) (Schneider et al., 2022). In this study,
432   we use the MUSICA retrievals from the Infrared Atmospheric Sounding Interferometer (IASI)
433   onboard METOP due to its broad spatiotemporal coverage, vertical profiling capability, and the
434   availability and accessibility of its dataset (Diekmann et al., 2021). It has a horizontal footprint
435   of approximately 12 km at nadir (directly below the satellite), increasing with the angle of
436   observation. This configuration ensures nearly global coverage twice daily.

437   In this study, as no satellite retrievals of δ^{18}O are currently available, we compared our
438   observed vapor δ^{2}H profiles up to the upper troposphere with satellite observations. Due to the
439   intermittent availability of IASI data at any given location, we limited our comparison of
440   observational results across various altitudes at our study site to days when IASI data were
441   available. Satellite measurements, particularly for vertical profiles of water vapor isotopes, are
442   inherently different from direct sampling, they represent a vertical average over layers
443   determined by the averaging kernels (Rodgers and Connor, 2003; Worden et al., 2006).
444   Therefore, their comparability with ground-based or drone-based observations, which provide
445   high-resolution local data, is limited. The MUSICA retrievals from the IASI satellite instrument
446   provides water vapor isotope data at three altitude levels: 1-3 km in the lower troposphere, 4-7
447   km in the mid-troposphere, and 8-12 km in the upper troposphere. Given that our study started
448   at an altitude of 3856 m, we used the retrieved δ^{2}H data for the 4–7 km and 8–12 km levels.
449   However, these measurements represent a vertical average over layers determined by the

450 averaging kernels (Rodgers and Connor, 2003; Worden et al., 2006). While using averaging
451 kernels to smooth the observed profile could facilitate a more quantitative analysis, the multi-
452 level data with averaging kernels for 2020 are not publicly available, we therefore simply
453 averaged the observations for the corresponding altitudes. Consequently, the comparison
454 remains mainly qualitative.

4 Results

4.1 Parameter estimates

457 The $\lambda_{surface}$ was determined through laboratory Experiment No. 1. Based on Eq. 10, the
458 parameter $\lambda_{surface}$ was estimated to be 0.0312 (uncertainty range: 0.0291 to 0.0317) for the 0.5
459 L air bags and 0.0255 (uncertainty range: 0.0250 to 0.0259) for the 4 L air bags (Fig. 3a, Table
460 1).
461 The isotopic fractionation coefficients α, were determined through laboratory Experiment
462 No. 2. From the averaged results of these measurements, using Eq. 13, the water vapor isotopic
463 exchange coefficient, expressed as λ/α, was estimated to be 0.0249 for ^{18}O and 0.0244 for ^{2}H
464 (Fig. 3b and c). Consequently, $\alpha_{^{18}O}$ was estimated to be 1.0241 (0.0255/0.0249), and $\alpha_{^{2}H}$
465 was estimated to be 1.0451 (0.0255/0.0244) (Fig. 3b and d). Two additional sets of fractionation
466 coefficients α, were obtained: $\alpha_{^{18}O} = 1.0254$, $\alpha_{^{2}H} = 1.0506$, and $\alpha_{^{18}O} = 1.0264$, $\alpha_{^{2}H} =$
467 1.0380 (Table 1).
468 The specific parameter values obtained in this study pertain to the Teflon air bags used in
469 the aforementioned tests, conducted at an ambient temperature of 16°C. These values depend
470 on bag material, temperature, and pressure, which should be considered when applying the
471 model under different conditions. We also noted batch-to-batch variations among air bags from
472 the same manufacturer. We apply α measured under ground-level storage and measurement
473 conditions, assuming negligible temperature and pressure effects during the short (10–20 min)
474 drone-based sampling period. Future work is needed to quantify these dependencies.
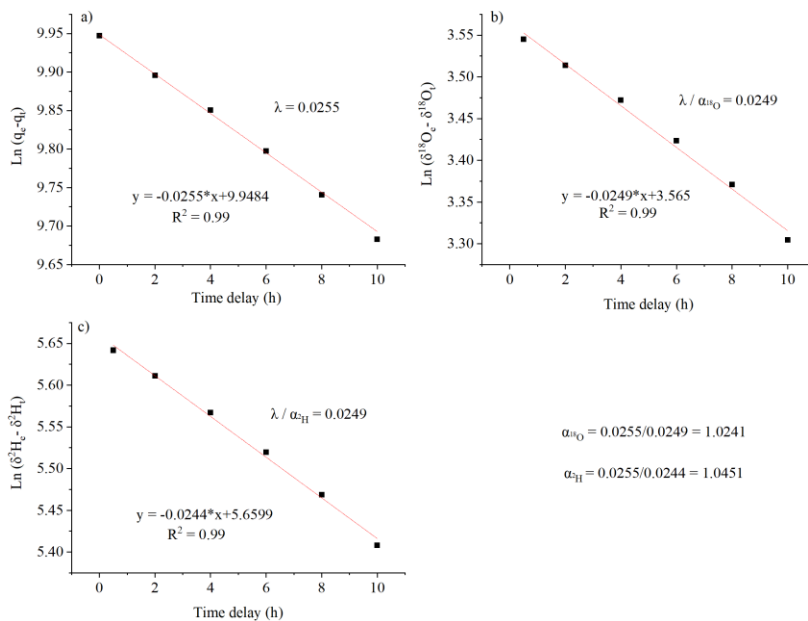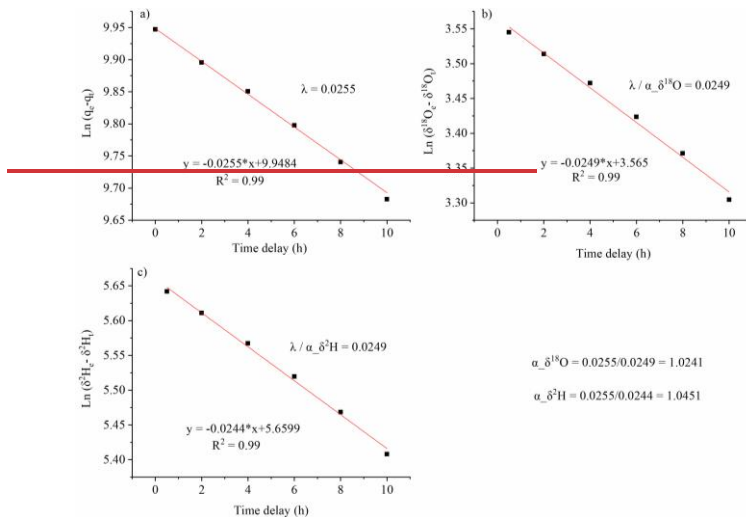
Figure 3 Determination of 3 parameters of the diffusion model : $\lambda_{surface}$ (a) from Experiment No. 1, $\alpha^{18}O_{18O}$ (b), and $\alpha^2H\alpha_{2H}$ (c) from Experiment No. 2.

     ## 4.2 Diffusion model validation

478   ### 4.2.1   General case

479
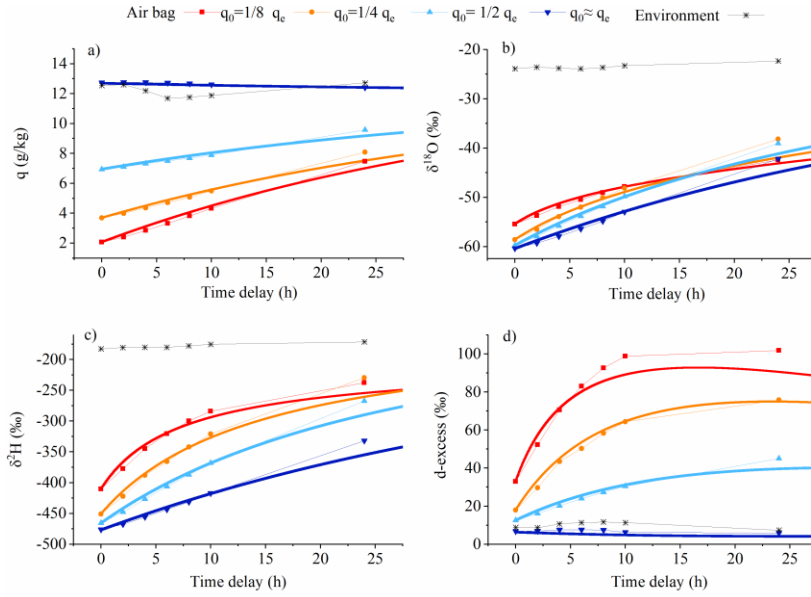
Figure 4: Comparison of the variation within the air bag over time in laboratory permeability experiments (markers) and diffusion model simulations (lines) across a range of initial humidities at t = 0 (q_0), ranging from approximately 1/8 * q_e to q_e (q_e denotes the environmental humidity), under the condition that the water vapor isotopic composition in the air bag significantly differs from ambient values : a) humidity; b) $\delta^{18}O$; c) δ^2H, d) d-excess.

480   To validate the model, we used Experiment No.3 described in Subsection 3.2. The
481 diffusion model simulations (lines in Figs. 4, 5, 6, and Fig. A2) are in close agreement with our
482 experimental observations (markers in Figs. 4, 5, 6, and Fig. A2), showing consistency in
483 humidity, $\delta^{18}O$, δ^2H, and d-excess variations, with only minor deviations. Shorter storage times
484 produce fewer deviations. When the humidity inside the air bag is lower than the ambient level,
485 vapor from the environment enters the air bag, resulting in a gradual increase in humidity (Fig.
486 4a and Fig. A2). Meanwhile, because the water vapor isotopic composition in the air bag is
487 significantly lower than the ambient values, $\delta^{18}O$ and δ^2H in the air bag gradually increase and
488 toward ambient values as ambient moisture enters the bags over time (Fig. 4b and c). In contrast,
489 the d-excess increase as the time delay progresses due to kinetic fractionation during moisture
490 diffusion into the air bag (Fig. 4d), as detailed in the following Subsection 4.2.2.
491   We observed that some curves unexpectedly intersect, which can be understood by
492 analyzing Eq. 8. The first term ($\frac{\lambda}{\alpha} * (R_e - R_{(t)})$) continuously drives $R_{(t)}$ towards R_e, while the

493   second term $(\frac{\lambda}{q(t)}*(q_e-q_{(t)})*(\frac{R_e}{\alpha}-R_{(t)}))$ modulates the rate of change. Initially, for simulations

494   with lower q_0 (e.g., the red and orange curves), $q_e-q_{(t)}$ is large, making the second term

495   significant and positive, thereby increasing $R_{(t)}$ more rapidly. However, as $R_{(t)}$ exceeds R_e/α, the

496   sign of this term reverses, slowing down the increase in $R_{(t)}$ compared to other curves. In

497   contrast, curves with higher initial q_0 (e.g., blue curve) experience a steadier growth and

498   eventually surpass the initially faster-growing curves, leading to the observed crossing.

499   **4.2.2   Particular cases**

500
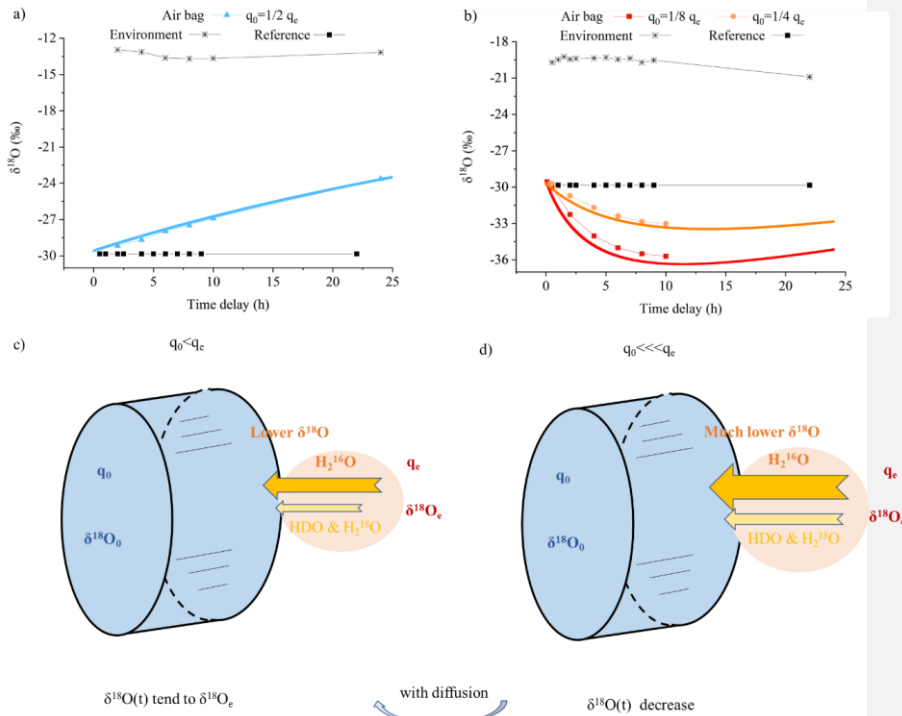
Figure 5   (a-b) Variations of $\delta^{18}O$ under different conditions: (a) when both the differences between internal ($\delta^{18}O_0$) and external ($\delta^{18}O_e$) $\delta^{18}O$ as well as between internal (q_0) and external (q_e) humidity are not significant, $\delta^{18}O$ gradually increases toward equilibrium; (b) when q_0 is significantly lower than q_e, a stronger vapor influx causes enhanced kinetic fractionation, leading to a decrease in $\delta^{18}O$. (c-d) Corresponding schematics: (c) illustrates the mechanism for (a), where a weaker humidity gradient results in slower isotopic shifts, while (d) corresponds to (b), showing intensified fractionation with a larger gradient, with arrows indicating vapor flux direction and fractionation intensity. $\delta^{18}O$ (t) is the variation of $\delta^{18}O$ within the air bag over time. In (a) and (b), the colored lines represent model simulations based on Eq.8, using parameterization from Experiments No. 1 and 2. Colored square markers show the corresponding experimental observations within the air bags. Black square markers

501   Due to isotopic kinetic fractionation, lighter $H_2^{16}O$ molecules preferentially diffuse into
502 the air bag compared to heavier isotopologues such as $HD^{16}O$ and $H_2^{18}O$, resulting in a vapor
503 flux with lower $\delta^{18}O$ relative to ambient vapor (Fig. 2). Moreover, variations within the air bag
504 are driven by differences in water vapor content and isotopic ratios between its interior and
505 exterior, as described in the diffusion model in Section 2. As shown in the initial experiment
506 (Fig. 4b and c), when the internal $\delta^{18}O$ and $\delta^{2}H$ are significantly below the ambient values, the
507 δ-values of the diffusing vapor, although lower than ambient, still exceeds the initial internal δ-
508 values, leading to a gradual increase towards the ambient values; diffusion simply equilibrates
509 the isotopic composition in the bag and the environment. When the disparity between internal
510 and external $\delta^{18}O$ or $\delta^{2}H$ is not very substantial, and humidity differences are also minimal, the
511 weaker diffusive gradient produces less net kinetic fractionation. This results in a small amount
512 of vapor with lower $\delta^{18}O$ and $\delta^{2}H$ than the ambient moisture entering preferentially, but not
513 falling below internal initial values, thereby still drives a progressive increase in the internal
514 values towards ambient moisture (Fig. 5a and c). In contrast, with the same initial contrast
515 between internal and ambient δ-values, that is, the disparity between internal and external $\delta^{18}O$
516 and $\delta^{2}H$ is less pronounced, but q_o is much lower than q_e, there is a stronger net flux into the
517 bag, and this flux fractionates more rapidly; much more vapor with significantly lower $\delta^{18}O$
518 and $\delta^{2}H$ than the ambient moisture (and lower values than the initial internal vapor) enters the
519 air bags and dominates their isotopic composition, thereby reducing the internal δ-values
520 (Fig.5b and d). The smaller the difference in humidity and isotopic composition between the
521 inside and outside of the air bag, the slower and smaller the isotopic change in the vapor within
522 the air bag (Fig. 5 and Fig. 6).

523

524
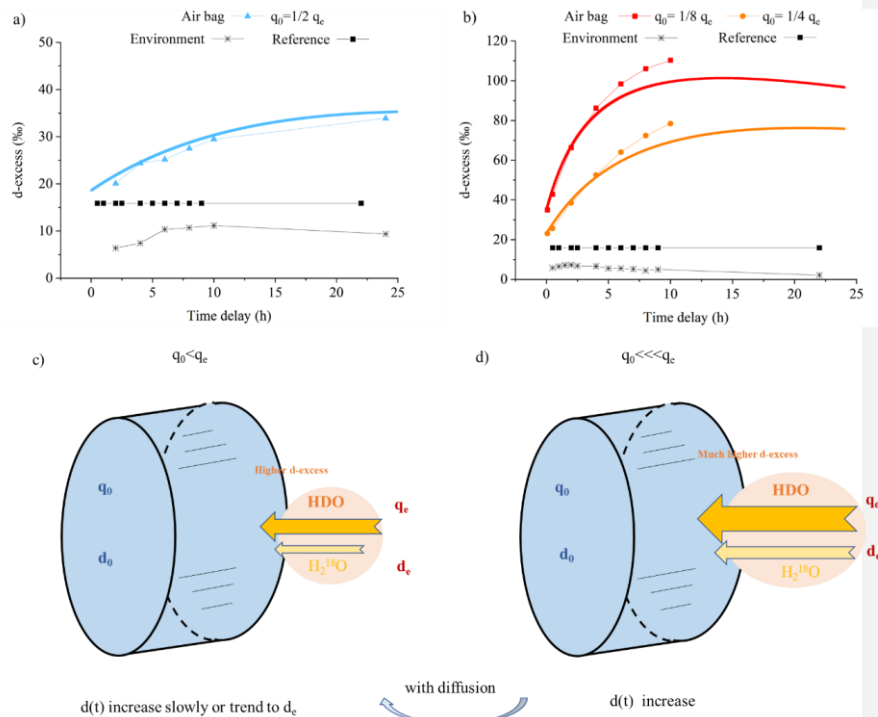
*Figure 6 (a-b) Same as Fig.5, but showing the evolution of d-excess: (a) when the difference
between the humidity inside (q_0) and outside (q_e) the air bag is not significant, d-excess
increases gradually; (b) when q_0 is significantly lower than q_e, a stronger vapor influx
enhances kinetic fractionation, causing a more rapid d-excess increase. (c-d) Corresponding
schematics: (c) illustrates the mechanism for (a), where a smaller humidity gradient results in
slower isotopic shifts, while (d) corresponds to (b), showing intensified fractionation with a
larger gradient. d_0 indicates the initial d-excess at t = 0, d_e represents the d-excess in the
environment. d(t) denotes the variation of d-excess within the air bag over time.*

In addition, because HDO and $H_2^{18}O$ diffuse at similar rates the magnitude of the kinetic
fractionation for D and ^{18}O is similar. However, since d-excess reflects deviations relative to
the 8:1 fractionation ratio typical of equilibrium processes, the tendency is for kinetic
fractionation during diffusion to contribute vapor with high d-excess and cause an increase in
d-excess during air bag storage as water vapor is added to the bag (Fig. 6a and c). When the
humidity difference between the inside and outside of the air bag increases, the d-excess of the
incoming vapor flux increases as a result of more intensive kinetic fractionation. This leads to
a faster increase in the vapor d-excess inside the air bag (Fig. 6b and d).

Regardless of the differences in water vapor humidity and isotopic compositions inside
and outside the air bag, the diffusion model simulations closely match the experimental
observations (Figs.4, 5 and 6). Using the method described in Subsection 3.4.2, the average
difference between all simulations and experimental data for each parameter represented the

545 model-experiment mismatch: 0.5 ‰ for $\delta^{18}O$, 4.1 ‰ for δ^2H, and 2.9 ‰ for d-excess.

546 ### 4.3 Raw and corrected vertical profiles

547 Here, we present a summary of drone-based observations from the field campaign at Mount
548 Laojun, Lijiang, on the southeastern edge of the Tibetan Plateau and the northwestern of the
549 Yunnan-Guizhou Plateau, China, conducted between June 25, 2020, and October 17, 2020.

550
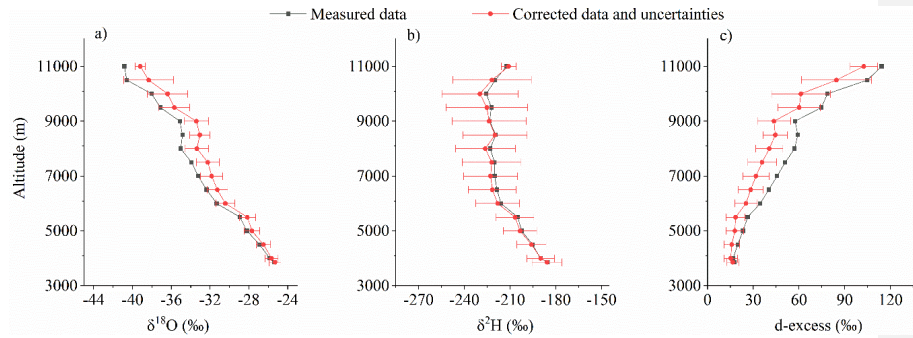
*Figure 7 Comparison of vertical profiles for the mean values of all raw measurements
and corrected data from June to October, and associated uncertainties for $\delta^{18}O$ (a), δ^2H (b)
and d-excess (c).*

551 As altitude increases, vapor $\delta^{18}O$ and δ^2H decrease due to condensation and precipitation
552 processes that occur as air masses ascend, which preferentially remove heavier isotopes
553 following Rayleigh distillation (Dansgaard, 1964). Meanwhile, the d-excess rises. This pattern
554 aligns with previous observations in the lower troposphere (He and Smith, 1999; Salmon et al.,
555 2019) and simulations of complete vertical profiles (Bony et al., 2008).
556 In our observations, the variation in $\delta^{18}O$ across the vertical profile from ground level at
557 3856 meters to 11 km is approximately 10-15‰. However, as altitude increases, the air becomes
558 progressively drier, leading to a greater disparity in humidity between the air collected in the
559 air bag and the surface storage environment. This aligns with the variations in Subsection 4.2.2
560 (Figs. 5b, 5d, and 6b, 6d). The strong kinetic fractionation driven by the diffusion of air into the
561 air bag results in a decrease in the water vapor $\delta^{18}O$ within the bag. After applying model
562 corrections, the corrected $\delta^{18}O$ inside the bag increased slightly compared to pre-correction
563 levels. As described in Subsection 4.2, vapor flux with higher d-excess entering the bag
564 increases the d-excess inside. As a compensation, the diffusion model applies corrections,
565 resulting in a reduced d-excess after correction (Fig. 7c and 10).

566 ### 4.4 Uncertainty estimates

567 According to the method of uncertainty estimation elaborated in Subsection 3.4.2, we
568 investigated~~determined the ranges for~~ four errors sources to evaluate uncertainty (Table 1).
569

570

571
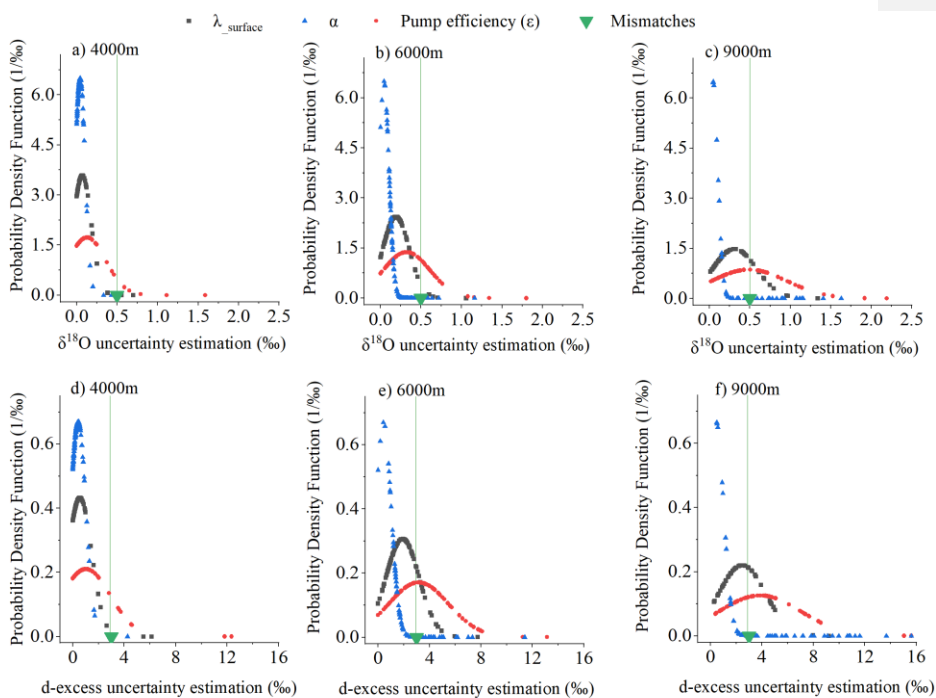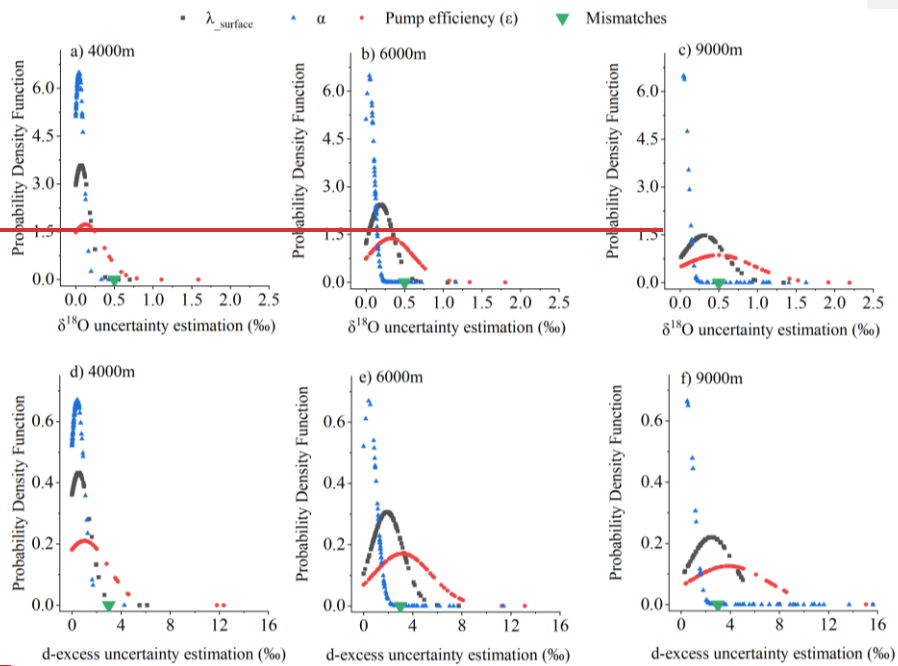
Figure 8: Contributions of different sources of uncertainty for $\delta^{18}O$ (a, b, c for 4000m, 6000m, 9000m, respectively) and d-excess (d, e, f for 4000m, 6000m, 9000m, respectively). The green triangle shows the average mismatch between the model and experimental results. The peak position of each probability density function (PDF) represents the most likely uncertainty value for a given source, while the width of the distribution reflects the variability.

(Fig. 8). Each PDF peak indicates the most probable uncertainty value, while its width reflects sensitivity to that parameter. Narrow PDFs suggest stable, well-constrained uncertainty sources, whereas broader PDFs indicate greater variability and a more diffuse impact on the correction outcome. The mismatch between the model and the experiment (green marker), calculated using the method described in Subsection 3.4.2, is assumed to remain constant across all altitudes. The other three error sources manifest as unimodal normal distributions at various altitudes for both $\delta^{18}O$ and d-excess. Errors due to uncertainties in pump efficiency (ε) are the main source, exhibiting the largest spread (Fig. 8) and increasing with altitude (Fig. 9). Errors derived from $\lambda_{surface}$ and α also increase with altitude (Figs. 8 and 9). As a result, at higher elevations, the satellite $\delta^{2}H$ differs more from the measured and corrected data than at lower altitudes (Fig. 10). This pattern arises because λ_{alt} deviates more from $\lambda_{surface}$ at higher elevations (Eq. 16), primarily due to increased errors in estimating M_{alt}, amplifying correction errors. Moreover, the humidity and isotopic disparity between the air captured in the air bag and lower-altitude ambient air widens with altitude, requiring more intensive corrections. Consequently, both the uncertainty (Figs. 8 and 9) and the magnitude of the diffusion correction (Fig. 7) increase with altitude.
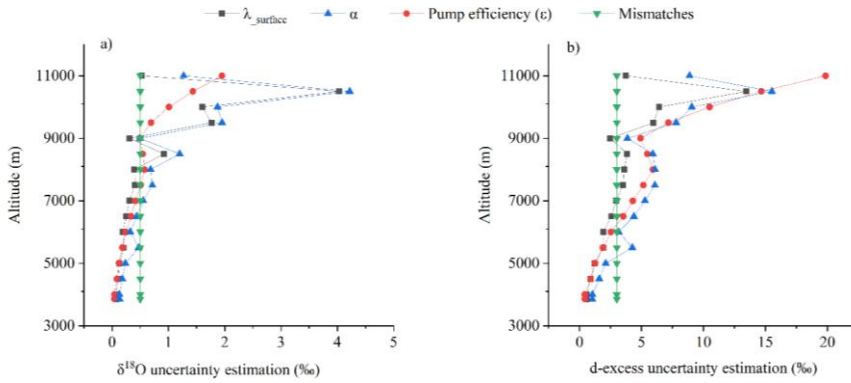
Figure 9 Mean uncertainty of $\delta^{18}O$ (a) and d-excess (b) with altitude for different sources.

On the contrary, errors pertaining to $\lambda_{surface}$ and α diminish at altitudes exceeding 10,500 meters. This phenomenon may be attributed to our sampling methodology. Although we collected air samples in sequence from low to high altitudes, these samples were measured in reverse order, from high to low altitudes. Consequently, samples taken from the highest altitudes had the shortest storage durations, typically ranging from 10 minutes to two hours.

Additionally, we extended the sampling times with increasing altitude (Fig. A1). These extended sampling periods and reduced storage durations help to partially offset the amplified disparities observed between the raw and corrected profiles at higher altitudes. During the drone-based sampling period, which lasted around 10-20 minutes, the external conditions impacting the air bags were not the ground-level environmental values used in the model but rather those of the vertical profile. However, the humidity at higher altitudes is lower than at ground level, and the isotopic composition are closer to those inside the airbag. Consequently, its impact on the airbag's internal conditions is less significant than suggested by using ground-level environmental values. Therefore, the overestimated error in our model accounted for these potential discrepancies.

The combined uncertainty from all sources, including $\lambda_{surface}$, α, pump efficiency (ε), and model-experiment mismatches, result in a total uncertainty of approximately 1‰ for $\delta^{18}O$ and 8‰ for d-excess across 98% of the data. The corresponding 95% confidence intervals are approximately 0.9‰ for $\delta^{18}O$ and 6.9‰ for d-excess. These This ranges is acceptable when compared to the substantial vertical variations we observed (~20‰ for $\delta^{18}O$ and ~100 ‰ for d-excess). Among these sources, ε contributes the largest uncertainty, particularly at higher altitudes (Fig. 8), likely due to the conservative uncertainty range we applied to account for potential reductions in collected air mass at high altitudes. Additionally, $\lambda_{surface}$ and α also contributes considerably to the total uncertainty (Figs. 8 and 9). To mitigate this, we recommend conducting multiple measurements to obtain an averaged value and performing repeated parameter validation to ensure robustness.

4.5 Comparison with Picarro measurements and satellite data
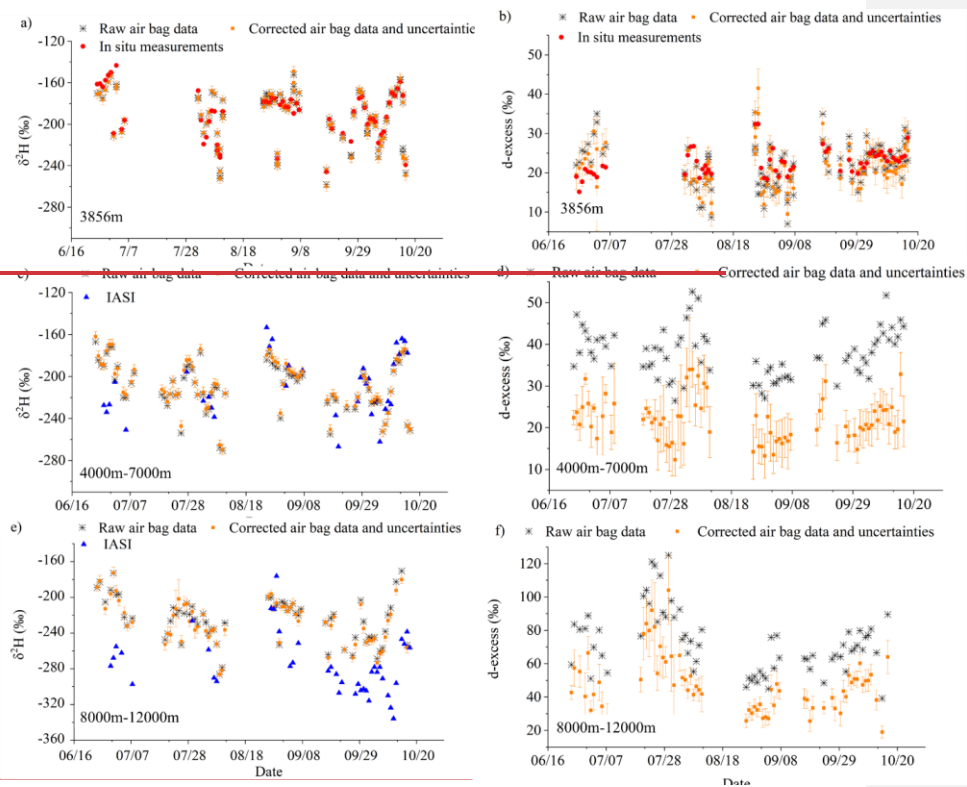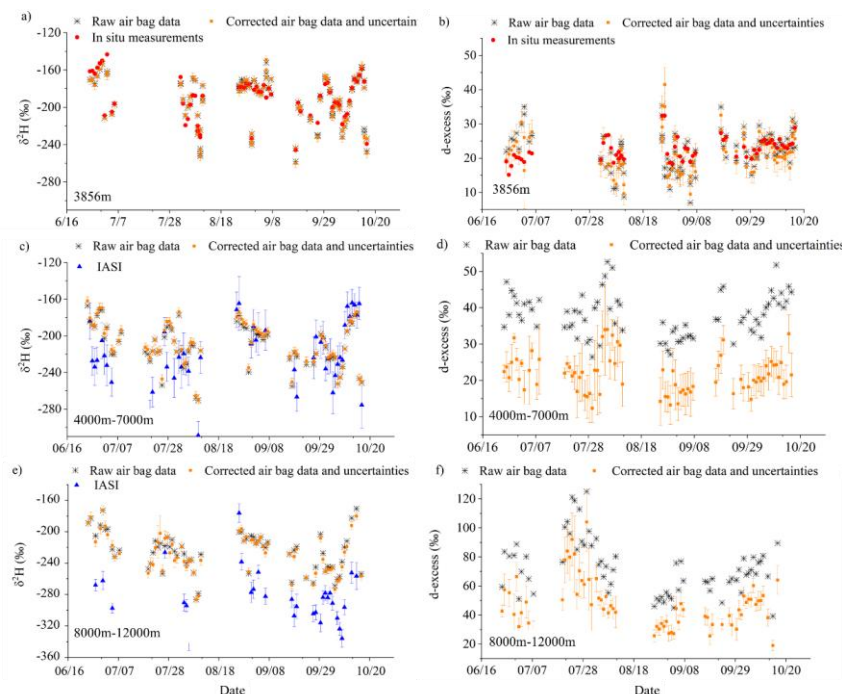
Figure 10 Time series comparison for δ²H (a, c, e) and d-excess (b, d, f):

(a, b) Raw and corrected (with uncertainties) instantaneous air bag measurements at the surface (3856 m), compared with Picarro in-situ measurements at the same altitude, averaged over the sampling period~~(legend: in situ measuremeents)~~.

(c, d) Raw and corrected (with uncertainties) altitude-averaged air bag measurements from 4000 m to 7000 m, compared with satellite data (IASI), which also include uncertainty ranges accounting only for retrieval-fit noise and the atmospheric temperature a priori constraint.

(e, f) Raw and corrected (with uncertainties) altitude-averaged air bag measurements from 8000 m to 12000 m, compared with satellite data (IASI).

The left panel of Fig.10 (Figs. 10 a, c, and e) shows the comparison of raw and corrected water vapor δ²H measurements at different altitudes with in-situ surface-level measurements on the Picarro or IASI satellite data at corresponding altitudes.

At near-ground level, both the raw and corrected δ²H and d-excess values from the bag measurements show close agreement with the in-situ Picarro observations (Fig. 10a and b), indicating minimal diffusion effects under nearly identical humidity and isotopic conditions between the inside and outside of the bags. Most data points are distributed along the 1:1 line (Fig. A3), while d-excess shows slightly larger scatter. After applying the correction, the agreement improved: the correlation coefficient between the bag and Picarro δ²H values increased from 0.90 to 0.99, and for d-excess from 0.41 to 0.72. The mean absolute error (MAE)

between the corrected bag and Picarro measurements is 3.0‰ for δ^2H and 1.4‰ for d-excess. These discrepancies are within the uncertainty range derived from laboratory diffusion experiments and model–experiment mismatches, which were comprehensively incorporated in the error estimation (Sections 3.2 and 3.4): 0.5 ‰ for $\delta^{18}O$, 4.1 ‰ for δ^2H, and 2.9 ‰ for d-excess. The differences also ~~There is agreement between the raw measurements and corrected δ^2H and the in-situ δ^2H observed directly by Picarro at ground level (3856m), with a mean absolute error of 2.99 ‰ (Fig.10a, Fig.A3). The remaining minor differences~~ can be attributed to the fact that the Picarro in-situ observations are period-averaged, whereas the bag samples represent instantaneous values.

To compare corrected measurements with ~~independent~~ observations at higher altitudes, we refer to the IASI satellite dataset. We acknowledge that this comparison is qualitative, as satellite data represent vertical averages over layers defined by averaging kernels, and therefore differ in measurement footprints (both horizontal and vertical) and spatio-temporal sampling disparities (Shi et al., 2020). A more quantitative analysis could be facilitated if an averaging kernel is used to smooth the observed profiles (Herman et al., 2014), but even after such adjustment, substantial differences would likely persist. IASI provides only two overpasses per day (around 09:30 LT AM and PM), whereas our drone-based measurements were conducted locally during daytime. The IASI footprint (~12 km at nadir) provides coarse spatial averaging, whereas our measurements are local and instantaneous, limiting its ability to capture fine-scale variability at the sampling site. Importantly, IASI cannot observe through or below thick clouds such as anvils, and thus mainly samples air outside convective detrainment regions. Because convective detrainment isotopically enriches vapor (Kuang et al., 2003; Moyer et al., 1996; Smith et al., 2006; Vries et al., 2021; Webster and Heymsfield, 2003), the air masses observed by IASI—being farther from detrainment—are expected to be more depleted. This cloud-sampling limitation may therefore contribute to the lower δ^2H values retrieved by IASI in the upper troposphere compared with our in-situ observations. Such fundamental mismatches in vertical weighting, temporal coverage, and spatial representativeness are noted in previous satellite–in-situ intercomparisons, which found that satellites capture large-scale isotopic gradients but smooth out fine-scale vertical and diurnal variations (Herman et al., 2014; Lacour et al., 2018). These complementary characteristics highlight the value of combining satellite and high-resolution in-situ observations: satellites provide synoptic coverage, while local observations resolve small-scale processes that shape the isotopic structure of the atmosphere. Overall, our comparison with IASI should thus be regarded as a qualitative consistency check confirming large-scale and temporal coherence rather than a one-to-one correspondence.

~~F~~For most intervals, IASI satellite data closely match~~es~~ raw and corrected δ^2H measurements for altitudes 4000–7000m. In the 8000–12000m range, although applying the diffusion correction increased the correlation coefficient between the air-bag observations and the IASI data from 0.53 to 0.60, IASI data ~~is~~ are lower than δ^2H air-bag observations during certain periods, particularly June and September 2020; one possible reason is unaccounted environmental influences at high altitudes~~.~~. However, it is noteworthy that ~~While~~ the IASI data closely match~~es~~ the observed δ^2H for all other periods in the 4000–7000 m~~eter~~ range, ~~it is~~they are also lower in June 2020. ~~A more quantitative analysis could be facilitated if an averaging kernel is used to smooth the observed profiles (Herman et al., 2014). All comparisons reflect consistent temporal variations.~~ Moreover, diffusion within the sampling bags could, in principle,

introduce systematic bias, yet the IASI values sometimes agree well, sometimes appear higher, and sometimes lower than our measurements (Fig. 10). Therefore, the differences between our in-situ observations and the IASI retrievals likely arise mainly from representativeness differences intrinsic to the satellite data, as discussed above—practically the cloud-sampling limitation in the upper troposphere—rather than from diffusion-related biases. Accordingly, such variations cannot be corrected by the diffusion model, which accounts for isotopic fractionation during air-bag storage but not for spatiotemporal or cloud-sampling discrepancies between observation platforms.

The right panel of Fig.10 (Figs. 10 b, d, and f) shows the comparison of raw and corrected vapor d-excess measurements. As expected for near-surface sampling (Fig. b), the differences between the bag samples and the ambient values are very small, and the impact of diffusion is minimal. Consequently, the applied corrections are also small. After correction, the a mean absolute error is 1.37‰. . For the 4000–7000m and 8000–12000m observations, nNo d-excess dataset is available for comparison for the 4000–12000m (Fig. 10d and f). As previously noted, corrected d-excess values should be and are lower than the raw data, as expected from diffusion theory. As previously noted, raw d-excess are higher than corrected data due to kinetic fractionation. After correction, d-excess decreases. For the 8000–12000 m observations, the correction magnitude is relatively smaller than at lower altitudes due to the shorter storage time of the air bags. But

Although no completely independent dataset is available for direct validation, our model—already verified by laboratory experiments—was used to perform a detailed assessment of all potential error sources and to quantify a comprehensive and conservative uncertainty range of the corrected data.—

5 Conclusion

High spatial and temporal resolution water vapor isotope data are critical for understanding various hydrologic cycle processes. However, observations of vertical water vapor isotope profiles are scarce, particularly in the upper troposphere. Satellite-derived vapor isotope data are available only at limited vertical and temporal resolutions. Acquiring high-resolution water vapor isotope data, especially under conditions where direct measurements are difficult, has been a significant challenge for the water isotopes research community. This study demonstrates the potential of a drone-based air bag sampling method to overcome this challenge, and offers solutions for evaluating air bag suitability and addressing air bag permeability.

While air bags offer the advantage of sample collection, their inherent permeability can affect the sealing integrity of the samples, leading to potential contamination. The permeability of airbag materials varies, with some exhibiting lower levels. We recommend prioritizing the use of glass containers and air bags with the lowest permeability for collecting water vapor using portable devices. Additionally, it is essential to conduct the permeability experiments described in this article before any experimental undertaking. This involves storing water vapor with known isotopic composition in the portable collection device for an extended period and then re-measuring these values to assess or determine the device's permeability parameters.

To further address the permeability challenge, we developed a mathematical model to evaluate and correct for diffusion and isotopic fractionation, ensuring the reliability of vapor isotope measurements using air bags. Calibrated with parameters from laboratory experiments, our correction model reconstructs the initial isotopic composition of sampled vapor by using data from both the air bag and the surrounding environment, offers a potential solution to the prevalent permeability challenges. This model was rigorously validated against observational experiments conducted under varying conditions. We also applied this model to drone-collected samples at various pressures. By estimating uncertainty and comparing corrected data with in-situ surface-level measurements on the Picarro and satellite observations, we validated the reliability and applicability of drone-based water vapor isotope measurements.

Our drone-based sampling system, combined with the diffusion model, effectively addresses the limitations of traditional high-altitude water vapor measurement methods. It meets the need for lightweight equipment while providing a more economical, efficient, and flexible alternative to conventional approaches involving large aircraft, airships, and balloons. This approach enables us to exploit the benefits of drone-based air bag sampling at high altitudes and over long distances, while effectively mitigating its potential limitations. This strategy significantly broadens its potential applications across various environments, thereby enhancing the range and richness of data that can be gathered for water vapor isotope research.

This study was conducted under stable temperature and equal internal and external pressures during storage. We acknowledge that a formulation based on partial pressure of water vapor would be more general and could improve model applicability under varying temperature and pressure conditions. Future work could extend the model to account for these factors.

Appendix A

Table A1 Summary of experiments: diffusion parameter quantification, model validation and differences in experimental methods. $\lambda_{surface}$ denotes the water vapor exchange coefficient at the surface, α refers to the fractionation coefficient of isotopes, q_0 represents the initial vapor humidity in the air bags, and q_e corresponds to the environmental vapor humidity.

Experiment Number	Experimental purpose	Differences in experimental methods
No. 1	Quantification of $\lambda_{surface}$	Dry air in the air bags
No. 2	Quantification of α	Water vapor with known isotopic compositions in the air bags under the condition $q_0 = q_e$
No. 3	Diffusion model validation	Water vapor with varying isotopic compositions and humidity levels in the air bags

741
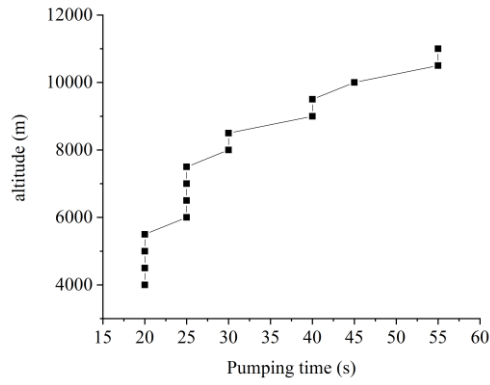
742 Figure A1 Sampling duration variation with altitude.

743
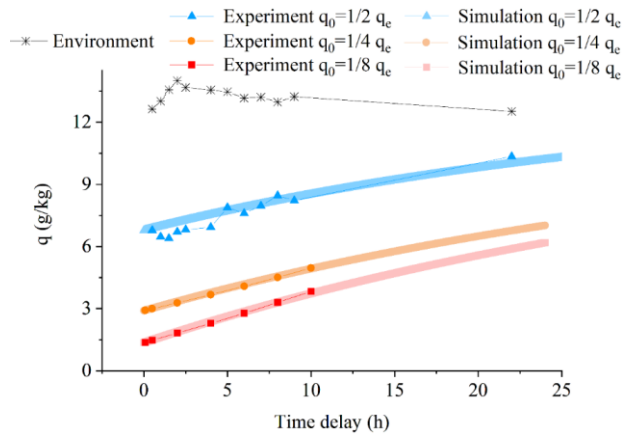
744   Figure A2 Comparison of humidity variation within the air bag over time in laboratory
745 permeability Experiments No.3 (markers) and diffusion model simulations (lines) for Figures
746 4 and 5. The experiments cover a range of initial humidities at $t = 0$ (q_0), from approximately
747                 $1/8 * q_e$ to $1/2\ q_e$, where q_e denotes environmental humidity.
748
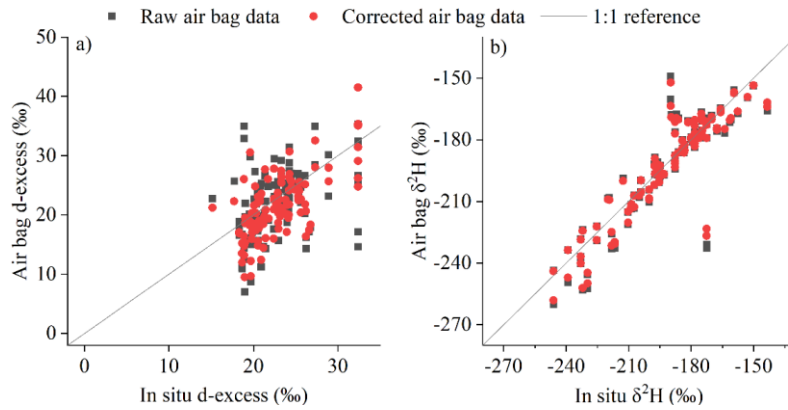
749
750 Figure A3 Comparison of raw and corrected air bag data with in situ observations averaged
751 over the sampling period (1:1 reference shown)

Code availability

753   The diffusion modeling code, which simulates the evolution of water vapor isotopes in the
754 airbag and corrects them to their initial values, is available at:
755   https://github.com/DishiWANG0608/Correcting-for-water-vapor-diffusion.git

Data availability

757   Data are available from the authors on request.

Video supplement

759 A video showcasing our field campaign on drone-derived water vapor isotope sampling up to
760 the upper troposphere (11 km) during convective activity, including the workflow for airbag
761 water vapor isotope sampling, is currently available upon request and will be publicly
762 accessible in the near future. Please contact the corresponding author for access
763 (di.wang@latmos.ipsl.fr).

Author contributions

765   D.W., C.R., and L.T. designed the research, established the subjects of the methodology,
766 and performed the analysis; D.W. and D.Y. conducted the observations; G.B., S.F., H.P. and
767 L.L. contributed to the establishment of methodologies, data calibration, and analysis; Y.S.
768 provided assistance with the computing; All authors contributed to the discussion of the results

769 and the final article; D.W. drafted the manuscript with contributions from all co-authors.

Competing interests

771 The contact author has declared that none of the authors has any competing interests.

Acknowledgments

773 The authors gratefully acknowledge the Infrared Atmospheric Sounding Interferometer
774 (IASI) for providing spatiotemporal coverage of δ^2H retrieval. We thank Jiaping Xu, Mingjian
775 Chen, Le Chan, and Yao Yao for their irreplaceable help in the development of the drones. We
776 are grateful to the management of 99 Dragon, Mountain Laojun in Lijiang for facilitating the
777 field experiments. We thank Pengbin Liang and Jiangrong Tai for partially participating in the
778 field observations. We acknowledge Hans Christian Steen-Larsen and Harald Sodemann for
779 their discussions on the correction method. We acknowledge the use of OpenAI's ChatGPT to
780 assist in refining the language. This work was supported by the National Natural Science
781 Foundation of China (Grants No. 42401043 and U2202208), the fellowship from the China
782 Postdoctoral Science Foundation (Grant No.2025T180092), the Strategic Priority Research
783 Program of the Chinese Academy of Sciences (Grant No. XDB40000000), and the Science and
784 Technology Department of Yunnan Province (Grant No. 202201BF070001-021). Di Wang
785 acknowledges support from Chinese Scholarship Council and the Postdoctoral Fellowship
786 Program of China Postdoctoral Science Foundation (Grant No. GZC20241440). Siteng Fan
787 acknowledges support from the Marie Skłodowska-Curie Actions of European Research
788 Executive Agency (Grant No. 101064814) and the High Level Special Fund of Southern
789 University of Science and Technology (Grant No. G03050K001).

References

791 Ayliffe, L., Cerling, T., Robinson, T., West, A., Sponheimer, M., Passey, B., Hammer, J., Roeder, B.,
792 Dearing, M., Ehleringer, J., 2004. Turnover of carbon isotopes in tail hair and breath CO 2 of horses fed
793 an isotopically varied diet. Oecologia 139, 11-22.
794 Bony, S., Risi, C., Vimeux, F., 2008. Influence of convective processes on the isotopic composition
795 (δ18O and δD) of precipitation and water vapor in the tropics: 1. Radiative-convective equilibrium and
796 Tropical Ocean–Global Atmosphere–Coupled Ocean-Atmosphere Response Experiment (TOGA-COARE)
797 simulations. Journal of Geophysical Research: Atmospheres 113.
798 Bowen, G.J., Cai, Z., Fiorella, R.P., Putman, A.L., 2019. Isotopes in the Water Cycle: Regional-to
799 Global-Scale Patterns and Applications. Annual Review of Earth and Planetary Sciences 47.
800 Brienen, R.J., Schöngart, J., Zuidema, P.A., 2016. Tree rings in the tropics: insights into the ecology
801 and climate sensitivity of tropical trees. Tropical tree physiology: adaptations and responses in a
802 changing environment, 439-461.
803 Cerling, T.E., Wittemyer, G., Rasmussen, H.B., Vollrath, F., Cerling, C.E., Robinson, T.J., Douglas-

804 Hamilton, I., 2006. Stable isotopes in elephant hair document migration patterns and diet changes.
805 Proceedings of the National Academy of Sciences 103, 371-373.

806 Dansgaard, W., 1964. Stable isotopes in precipitation. Tellus 16, 436-468.

807 Fick, A., 1855. Ueber diffusion. Annalen der physik 170, 59-86.

808 Galewsky, J., Steen-Larsen, H.C., Field, R.D., Worden, J., Risi, C., Schneider, M., 2016. Stable isotopes
809 in atmospheric water vapor and applications to the hydrologic cycle. Reviews of Geophysics 54.

810 Gat, J.R., 1996. Oxygen and hydrogen isotopes in the hydrologic cycle. Annual Review of Earth and
811 Planetary Sciences 24, 225-262.

812 Ghosh, P., Brand, W.A., 2003. Stable isotope ratio mass spectrometry in global climate change
813 research. International Journal of Mass Spectrometry 228, 1-33.

814 Gralher, B., Herbstritt, B., Weiler, M., 2021. Unresolved aspects of the direct vapor equilibration
815 method for stable isotope analysis (δ 18 O, δ 2 H) of matrix-bound water: unifying protocols through
816 empirical and mathematical scrutiny. Hydrology and Earth System Sciences 25, 5219-5235.

817 Grootes, P.M., Stuiver, M., 1997. Oxygen 18/16 variability in Greenland snow and ice with 10(-3)-
818 to 10(5)-year time resolution. Journal of Geophysical Research-Oceans 102, 26455-26470.

819 Havranek, R.E., Snell, K.E., Davidheiser-Kroll, B., Bowen, G.J., Vaughn, B., 2020. The Soil Water
820 Isotope Storage System (SWISS): An integrated soil water vapor sampling and multiport storage system
821 for stable isotope geochemistry. Rapid Communications in Mass Spectrometry 34, e8783.

822 He, H., Smith, R.B., 1999. Stable isotope composition of water vapor in the atmospheric boundary
823 layer above the forests of New England. Journal of Geophysical Research Atmospheres 104, 11657-
824 11673.

825 Hendry, M., Schmeling, E., Wassenaar, L., Barbour, S., Pratt, D., 2015. Determining the stable
826 isotope composition of pore water from saturated and unsaturated zone core: improvements to the
827 direct vapour equilibration laser spectrometry method. Hydrology and Earth System Sciences 19, 4427-
828 4440.

829 Herbstritt, B., Gralher, B., Seeger, S., Rinderer, M., Weiler, M., 2023. Discrete in situ vapor sampling
830 for subsequent lab-based water stable isotope analysis. Hydrology and Earth System Sciences 27, 3701-
831 3718.

832 Herman, R., Cherry, J., Young, J., Welker, J., Noone, D., Kulawik, S., Worden, J., 2014. Aircraft
833 validation of Aura Tropospheric Emission Spectrometer retrievals of HDO/H 2 O. Atmospheric
834 Measurement Techniques 7, 3127-3138.

835 Hodges, J.T., Lisak, D., 2006. Frequency-stabilized cavity ring-down spectrometer for high-
836 sensitivity measurements of water vapor concentration. Applied Physics B 85, 375-382.

837 Johnson, L., Sharp, Z., Galewsky, J., Strong, M., Van Pelt, A., Dong, F., Noone, D., 2011. Hydrogen
838 isotope correction for laser instrument measurement bias at low water vapor concentration using
839 conventional isotope analyses: application to measurements from Mauna Loa Observatory, Hawaii.
840 Rapid Communications in Mass Spectrometry 25, 608-616.

841 Kuang, Z., Toon, G.C., Wennberg, P.O., Yung, Y.L., 2003. Measured HDO/H2O ratios across the
842 tropical tropopause. Geophysical Research Letters 30.

843 Lacour, J.-L., Risi, C., Worden, J., Clerbaux, C., Coheur, P.-F., 2018. Importance of depth and intensity
844 of convection on the isotopic composition of water vapor as seen from IASI and TES δD observations.
845 Earth and planetary science letters 481, 387-394.

846 Magh, R.-K., Gralher, B., Herbstritt, B., Kübert, A., Lim, H., Lundmark, T., Marshall, J., 2022.
847 Conservative storage of water vapour–practical in situ sampling of stable isotopes in tree stems.

848   Hydrology and Earth System Sciences 26, 3573-3587.

849   Michener, R., Lajtha, K., 2008. Stable isotopes in ecology and environmental science. John Wiley &
850   Sons.

851   Millar, C., Pratt, D., Schneider, D.J., McDonnell, J.J., 2018. A comparison of extraction systems for
852   plant water stable isotope analysis. Rapid Communications in Mass Spectrometry 32, 1031-1044.

853   Moyer, E.J., Irion, F.W., Yung, Y.L., Gunson, M.R., 1996. ATMOS stratospheric deuterated water and
854   implications for troposphere-stratosphere transport. Geophysical Research Letters 23, 2385-2388.

855   Muccio, Z., Jackson, G.P., 2009. Isotope ratio mass spectrometry. Analyst 134, 213-222.

856   Rodgers, C.D., Connor, B.J., 2003. Intercomparison of remote sounding instruments. Journal of
857   Geophysical Research: Atmospheres 108.

858   Rozmiarek, K.S., Vaughn, B.H., Jones, T.R., Morris, V., Skorski, W.B., Hughes, A.G., Elston, J., Wahl,
859   S., Faber, A.-K., Steen-Larsen, H.C., 2021. An unmanned aerial vehicle sampling platform for atmospheric
860   water vapor isotopes in polar environments. Atmospheric Measurement Techniques 14, 7045-7067.

861   Salmon, O.E., Welp, L.R., Baldwin, M.E., Hajny, K.D., Stirm, B.H., Shepson, P.B., 2019. Vertical profile
862   observations of water vapor deuterium excess in the lower troposphere. Atmospheric Chemistry and
863   Physics 19, 11525-11543.

864   Shi, X., Risi, C., Pu, T., Lacour, J.l., Kong, Y., Wang, K., He, Y., Xia, D., 2020. Variability of isotope
865   composition of precipitation in the southeastern Tibetan Plateau from the synoptic to seasonal time
866   scale. Journal of Geophysical Research: Atmospheres 125, e2019JD031751.

867   Smith, J.A., Ackerman, A.S., Jensen, E.J., Toon, O.B., 2006. Role of deep convection in establishing
868   the isotopic composition of water vapor in the tropical transition layer. Geophysical Research Letters 33,
869   0_46-40_47.

870   Sprenger, M., Herbstritt, B., Weiler, M., 2015. Established methods and new opportunities for pore
871   water stable isotope analysis. Hydrological Processes 29, 5174-5192.

872   Steen-Larsen, H.C., Masson-Delmotte, V., Sjolte, J., Johnsen, S.J., Vinther, B.M., Bréon, F.M.,
873   Clausen, H.B., Dahl-Jensen, D., Falourd, S., Fettweis, X., 2011. Understanding the climatic signal in the
874   water stable isotope records from the NEEM shallow firn/ice cores in northwest Greenland. Journal of
875   Geophysical Research Atmospheres 116, 161-165.

876   Vries, A.D., Aemisegger, F., Pfahl, S., Wernli, H., 2021. Stable water isotope signals in tropical ice
877   clouds in the West African monsoon simulated with a regional convection-permitting model.

878   Wassenaar, L., Hendry, M., Chostner, V., Lis, G., 2008. High resolution pore water $\delta 2H$ and $\delta 18O$
879   measurements by H2O (liquid)– H2O (vapor) equilibration laser spectroscopy. Environmental science &
880   technology 42, 9262-9267.

881   Webster, C.R., Heymsfield, A.J., 2003. Water isotope ratios D/H, O-18/O-16, O-17/O-16 in and out
882   of clouds map dehydration pathways. Science 302, 1742-1745.

883   West, A.G., Goldsmith, G.R., Brooks, P.D., Dawson, T.E., 2010. Discrepancies between isotope ratio
884   infrared spectroscopy and isotope ratio mass spectrometry for the stable isotope analysis of plant and
885   soil waters. Rapid Communications in Mass Spectrometry 24, 1948-1954.

886   West, J.B., Bowen, G.J., Dawson, T.E., Tu, K.P., 2009. Isoscapes: understanding movement, pattern,
887   and process on Earth through isotope mapping. Springer.

888   Worden, J., Bowman, K., Noone, D., Beer, R., Clough, S., Eldering, A., Fisher, B., Goldman, A.,
889   Gunson, M., Herman, R., Kulawik, S.S., Lampel, M., Luo, M., Osterman, G., Rinsland, C., Rodgers, C.,
890   Sander, S., Shephard, M., Worden, H., 2006. Tropospheric emission spectrometer observations of the
891   tropospheric HDO/H2O ratio: Estimation approach and characterization. Journal of Geophysical

892 Research-Atmospheres 111.
893   Yu, W., Tian, L., Ma, Y., Xu, B., Qu, D., 2015. Simultaneous monitoring of stable oxygen isotope
894 composition in water vapour and precipitation over the central Tibetan Plateau. Atmospheric Chemistry
895 and Physics 15, 10251-10262.
896
897